

Electrocaloric Effect of Perovskite High Entropy Oxide Films

Yeongwoo Son,* Wanlin Zhu, and Susan E. Trolier-McKinstry

This paper describes two perovskite high entropy oxide (PHEO) compositions: Pb(Hf_{0.2}Zr_{0.2}Ti_{0.2}Nb_{0.2}Mn_{0.2})O₃ (Mn PHEO) and Pb(Hf_{0.2}Zr_{0.2}Ti_{0.2}Nb_{0.2}Al_{0.2})O₃ (Al PHEO). Powders are prepared by conventional solid state sintering by first pre-reacting the B-site oxides, then adding PbO. Phase pure Mn PHEO powder is obtained following calcination of the mixed powders at 750 °C for 240 min; however, secondary phases persisted in Al PHEO for heat treatments from 750 °C to 1200 °C. The Mn PHEO undergoes an entropy-driven phase transformation. Thin films of these compounds are synthesized by pulsed laser deposition (PLD) on a lead zirconate titanate seed layer on Pt-coated SiO₂/Si. The dielectric response of the Mn PHEO films show some contribution from space charge polarizability; in contrast, the Al PHEO films show a slim ferroelectric hysteresis loop and relaxor-like characteristics. The Al PHEO has a dielectric permittivity of ≈2000 with a loss tangent <0.05 from 100 Hz to 100 kHz; it has a dielectric maximum at 105 \pm 0.5 °C and a Burns' temperature of 234 \pm 0.5 °C. Indirect measurements based on the Maxwell-relations yielded a maximum electrocaloric temperature change of 8.4 K at 180 °C under the applied electric field of 1186 kV cm⁻¹.

1. Introduction

Rapid growth in the worldwide economy has led to concerns regarding global energy consumption and the environmental impact of increased greenhouse gas emissions.^[1] As of 2016, heating and cooling residential and public buildings accounted for approximately 12% of the total energy consumption in the United States.^[2] Given that many heating, ventilation and air conditioning (HVAC) systems are building wide, a considerable amount of energy is wasted heating or cooling empty spaces in buildings.^[3] Recently, personal thermal management has garnered attention as an alternative that can deliver precise, adjustable temperature control to a target area, reducing

Y. Son, S. E. Trolier-McKinstry
Department of Materials Science and Engineering and Materials
Research Institute
Penn State
University Park, PA 16802, USA
E-mail: yxs414@psu.edu
W. Zhu
Materials Research Institute
Penn State
University Park, PA 16802, USA

The ORCID identification number(s) for the author(s) of this article can be found under https://doi.org/10.1002/aelm.202200352.

DOI: 10.1002/aelm.202200352

wasted energy and increasing personal comfort. [4,5]

Such small-scale cooling is also of interest for on-chip cooling of semiconductor circuits.^[6] In 2020, data centers in the United State used an estimated 75 billion kWh, more than 2% of the nation's total energy consumption. Approximately half of this energy was spent on cooling these centers.[7] Advanced cooling technology that directly cools integrated circuits (ICs) (rather than the entire data center) offers an alternative. Furthermore, IC miniaturization has increased the power density of a packaged chip to 10⁶ W cm⁻² in 2018; power densities continue to rise, and often induce highly nonuniform heat generation.[8] It has been reported that more than 50% of IC failures are related to thermal control; this rate is expected to increase with further miniaturization.^[9] Therefore, new approaches for local cooling of IC are needed.[10]

Solid-state cooling, a potential solution, is highly compact, efficient, and environ-

mentally friendly. Research involving thermoelectric, electrocaloric, and magnetocaloric effects is promising.^[11–13] In 2006, large electrocaloric effects were observed in PZT thin films.^[14] Unlike magnetocaloric and barocaloric materials, the electrocaloric effect does not require bulky external magnets or pressure apparatus. Electrocalorics enable relatively good energy efficiency that can be further improved via charge recovery.^[15,16] Achieving large temperature changes in the electrocaloric material necessitates inducing large field-induced entropy changes. For this purpose, relaxor ferroelectrics are of special interest due to the disordered polarization and polar nanoregions.^[17]

A potential additional contribution to the entropy change in a ferroelectric-based material is to use high compositional complexity, e.g. through entropy engineering to further disorder the polarization on a local scale. In 2004, entropy stabilization of metallic alloys was introduced.[18,19] In 2015, the concept was broadened to include entropy stabilized oxides.^[20] Various entropy stabilized oxides (ESO) have shown high dielectric constants, superior ionic conductivity, and extremely high-temperature stability; that is, entropy stabilization provides an additional approach to property tunability with respect to enthalpy-based compositional design.[21-23] In cases where reversible phase transformations have not yet been demonstrated, potential ESO may be called high entropy oxides (HEO).[24] Triggered by the novel concept, several attempts to investigate the electrocaloric effect (ECE) based on HEO have been made. A-site disordered HEO ceramics show good

2199160x, 2022, 12, Downloaded from https://onlinelibrary.wiley.com/doi/10.1002/aelm.202200352 by Pennsylvania State University, Wiley Online Library on [16/05/2023]. See the Terms and Conditions (https://onlinelibrary.wiley

ns) on Wiley Online Library for rules of use; OA articles are governed by the applicable Creative Commons

temperature stability and a high ECE. $^{[25-27]}$ Moreover, high entropy polymeric films produced greatly enhanced ECE at 500 kV cm $^{-1}$. $^{[28]}$ In spite of the promising results, a study of ECE based on HEO film has been absent to date.

This paper discusses a new relaxor-type ferroelectric material based on entropy engineering and examines the effect of HEO-like formulations on electrocaloric responses. Pb was used for the A-site of the perovskite structure, while two different sets of compositions were used to populate the B-site. The first B-site precursor is based on hafnium (Hf), niobium (Nb), titanium (Ti), zirconium (Zr), and manganese (Mn), hereafter called the Mn precursor. After forming the perovskite phase, it is called the Mn perovskite high entropy oxide (Mn PHEO). Correspondingly, for the second B-site precursor, aluminum (Al) replaces Mn (Al PHEO). PZT was chosen as a starting composition with a large electrocaloric effect.^[14] Pb was fixed on the A-site because the lone electron pair promotes ferroelectricity.^[29] For the B-site, Hf, Zr, Ti, and Nb all have 3d⁰ electron configuration as ions, which facilitates development of ferroelectricity in the perovskite structure.^[30] Mn is a well-known Jahn-Teller ion that can induce lattice distortion which could be a source of additional entropy increase.

Al has no 3d electrons, so that it can play a role as a disrupter of polarization, which could also be a source of additional entropy change, while simultaneously maintaining charge balance on the B-site of the perovskite structure. Both powders and thin films were prepared.

2. Results and Discussion

2.1. PHEO Powder Processing

In order to reach a pseudo-cubic perovskite phase, in the PHEO compositions, the B-site precursor oxide powders were premixed and heat-treated following a columbite-like process.^[31] The results of heat treatment on the B-site powders are shown in Figure S1 (Supporting Information). Lead oxide powder and the pretreated B-site powder were mixed with a molar ratio of 1:1 and the batch was calcined. Several sequential heat treatments were performed to discover if a single phase could be developed and if entropy-driven cyclic phase transformations occurred. Figure 1A,B shows X-ray diffraction (XRD) patterns of the stoichiometric Mn PHEO and Al PHEO powders,

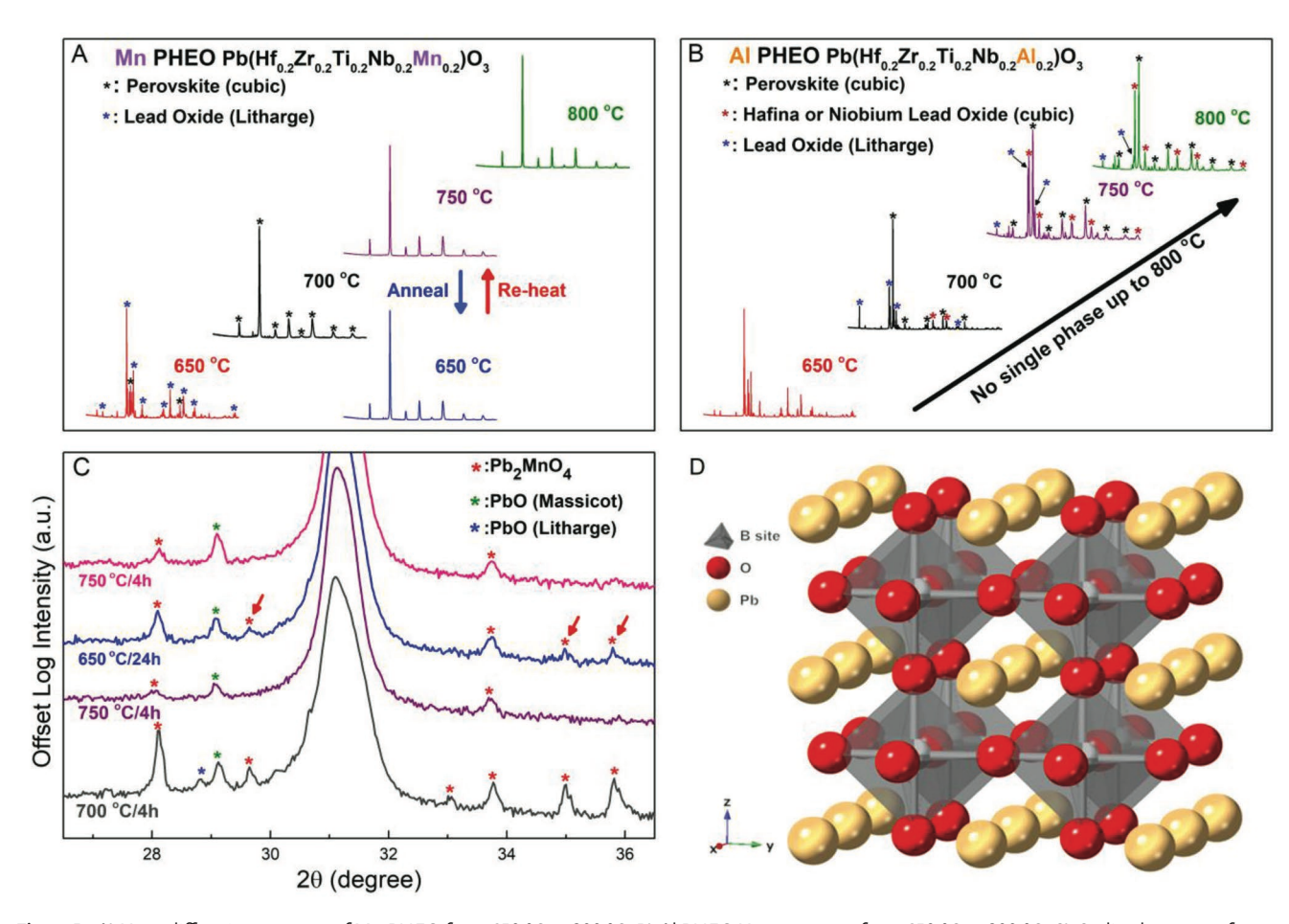


Figure 1. A) X-ray diffraction patterns of Mn PHEO from 650 °C to 800 °C. B) Al PHEO X-ray patterns from 650 °C to 800 °C. C) Cyclic phase transformation test of Mn PHEO and comparison based on the peaks around the perovskite 110 at \approx 31°. Red, green, and blue asterisks correspond to Pb₂MnO₄, PbO (Massicot), and PbO (Litharge), respectively. The peaks related to entropy-driven phase transformation are highlighted by red arrows. D) Crystal structure of pseudo-cubic perovskite high entropy oxide showing the B-site octahedra.

2199160x, 2022, 12, Downloaded from https://onlinelibrary.wiley.com/doi/10.1002/aelm.202200352 by Pennsylvania State University, Wiley Online Library on [16/05/2023]. See the Terms and Conditions (https://onlinelibrary.wiley.com/

ns) on Wiley Online Library for rules of use; OA articles are governed by the applicable Creative Commons License

47

respectively, heat treated from 650 °C to 800 °C, for 4 h periods. Litharge, cubic HfO₂ or niobium lead oxide (Pb_{1.5}Nb₂O_{6.5}), and perovskite peaks are marked with blue, dark red, and black asterisks, respectively. For the Mn PHEO calcined at 650 °C, clear litharge peaks appear, indicating unmixed lead oxide. With increasing temperature, the litharge peaks decreased in intensity, accompanied by the development of perovskite peaks at 700 °C. At 750 °C, the powder was predominantly perovskite phase with minimal second phase peaks at $\approx 28.1^{\circ},29.2^{\circ}$, and 33.7°. The lattice constant of Mn PHEO powder annealed at 750 °C calculated based on the Nelson–Riley method was 4.062 \pm 0.001Å (Figure S3 and Table S1, Supporting Information). [32]

After obtaining the perovskite phase at 750 °C, a cyclic phase transformation test was conducted at 650 °C for 24 h. This temperature minimized the volatility of the lead species; the longer annealing time off-set the resultant sluggish kinetics. Figure 1C highlights peaks around the perovskite 110 at \approx 31° 2 θ . The Mn PHEO powder was heat-treated at 750 °C for 4 h (purple), then annealed at 650 °C for 24 h (blue). The powder was reheated at 750 °C for 4 h (pink). The red arrows indicate several peaks which occur <700 °C and disappeared at >750 °C. Those peaks correspond to Pb2MnO4; it is prone to decompose into $Pb_{3}Mn_{7}O_{15} + PbO + Pb_{3}O_{4}$ between 700 °C and 750 °C. [33] The decomposition in the 750 °C temperature range results in a relatively weak intensity at ≈28.1° and 33.7°, and loss of the peaks at 29.6°, 35.0°, and 35.8°. In other words, the peaks marked by red arrows develop at ≤700 °C and the material is assimilated into the perovskite phase at temperatures ≥750 °C. The existence of the peaks implies the entropy-driven phase transformation of an ESO.^[24] The intensity of the entropy-driven secondary phase peaks is relatively weak due to slow kinetics of this transition.

For Al-HEO, cubic perovskite structure was obtained with some amount of unmixed lead oxide. With increasing temperature, the amount of unmixed lead oxide is reduced, but the intensity of peaks from cubic hafnia or niobium lead oxide $(Pb_{1.5}Nb_2O_{6.5})$ increases. Those peaks survive up to 1200 °C, hindering the formation of single phase of Al PHEO powder. Therefore, cyclic phase transformation data and lattice parameter calculations are not available for the Al PHEO.

2.2. PHEO Thin Films

To identify the best processing conditions for Mn PHEO films on Pt/Ti/SiO $_2$ /Si substrates, the laser frequency, substrate temperature, and deposition pressure were varied individually, while other conditions were held constant. The XRD results of the optimization process are shown in Figure S5 (Supporting Information). It was found that phase-pure Mn PHEO film could not be fabricated on Pt/Ti/SiO $_2$ /Si substrates for the range of conditions explored, as overlapping regions of Pb-rich pyrochlore or Pb-deficient pyrochlore phases occured. The best processing conditions for Mn PHEO films on the platinized silicon substrate are: 175 mTorr O $_3$ /O $_2$ deposition pressure, 10 Hz laser frequency, and substrate temperature of 630 °C.

To promote the formation of a single-phase perovskite film, a seed layer of 60 nm thick {100} oriented niobium doped lead zirconate titanate (PNZT) was grown on the Pt-coated Si substrate. PHEO films were then grown using the optimized conditions listed above. Figure 2A shows the XRD scans of Al PHEO (orange), Mn PHEO (violet), and the PNZT seed layer (black), respectively. Peaks from the substrate and other wavelengths from the X-ray source are marked with an asterisk (*). The films were grown to a thickness of ≈490 nm; this should minimize the impact of the seed layer on the electrical properties. It is clear that the highly oriented PNZT seed layer promotes formation of phase-pure Mn PHEO with no detected secondary phase. For Al PHEO films, the predominant peaks are from the perovskite phase, with a small pyrochlore peak at \approx 29.4 and additional weak peak at \approx 19° 2 θ . The XRD peaks from the Al PHEO film are well separated from those of the PNZT

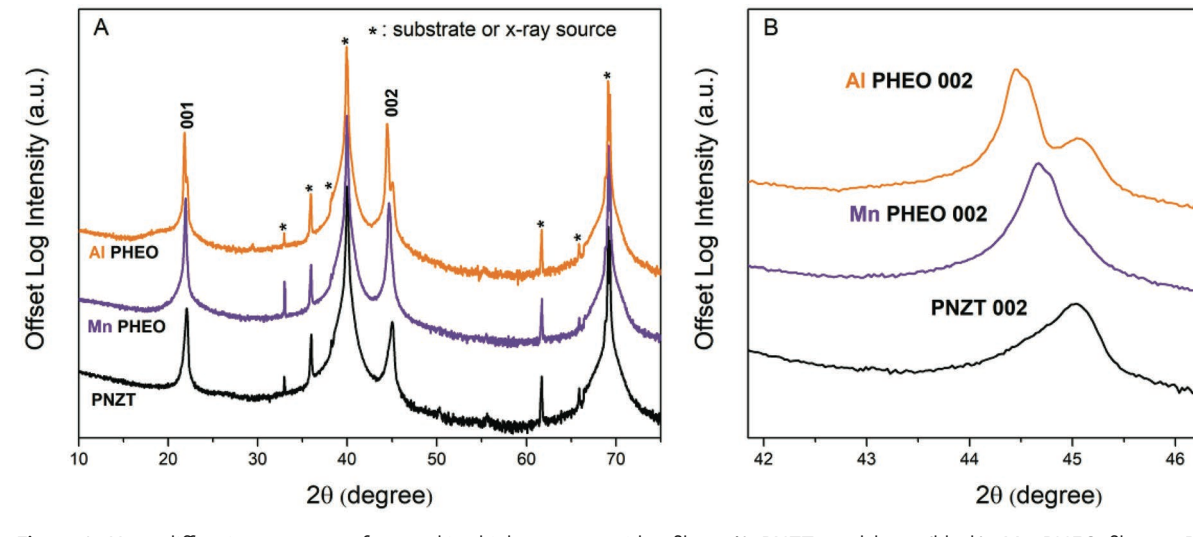


Figure 2. X-ray diffraction patterns of perovskite high entropy oxides films. A) PNZT seed layer (black), Mn PHEO film on PNZT seed layer (violet), and Al PHEO film on PNZT seed layer (orange). B) Enlarged view around {200} to highlight peak shifting between Al PHEO and Mn PHEO.

2199160x, 2022, 12, Downloaded from https://onlinelibrary.wiley.com/doi/10.1002/alm.202200352 by Pemsylvania State University, Wiley Online Library on [16/05/2023]. See the Terms and Conditions (https://onlinelibrary.wiley.com/terms-and-conditions) on Wiley Online Library for rules of use; OA articles are governed by the applicable Creative Commons Licenses

Table 1. Out-of-plane lattice parameters of PNZT seed layer, Mn PHEO film, Mn PHEO powder, and Al PHEO films.

	PNZT seed layer	Mn PHEO film	Mn PHEO powder	Al PHEO film
a[Å]	4.024	4.047	4.062	4.076

seed layer as shown in Figure 2B, while the peaks overlap in the Mn PHEO film. In particular, the {200} diffraction peak of the Al PHEO appears at a lower angle compared to the Mn PHEO, indicating a larger out-of-plane lattice parameter. This occurred even though Mn3+ has a larger Shannon-Prewitt ionic radius than Al3+ for octahedral coordination.[34] Table 1 shows the lattice parameters of the PNZT seed layer, Mn PHEO, Mn PHEO powder, and Al PHEO films, respectively. It is possible that the Mn ions occupied both B-site and A-site of the perovskite structure, or that much of the Mn adopted the 4+ oxidation state, reducing the lattice parameter significantly.[35,36] It is also possible that different levels of Pb vacancy concentration occurred in the Mn PHEO and Al PHEO films due to Pb volatility during vacuum processing. It should be noted here that the lattice parameter of Mn PHEO powder is larger than the out-of-plane lattice parameter of the corresponding film by 0.015 Å. This could be due to higher valence state of Mn or strain.

The surface microstructure and chemical analysis of Mn PHEO and Al PHEO films are shown in **Figures 3** and **4**, respectively. No distinguishable cracks or defects appear and the microstructure is dense, with average lateral grain sizes of 180 nm for both Mn PHEO and Al PHEO films. Boulders were seen on the surface of Al PHEO films, however, they were rarely seen on Mn PHEO films. Based on EDS results, both Mn PHEO and Al PHEO films were compositionally uniform with no segregation at the given length scale.

2.3. Room Temperature Dielectric and Ferroelectric Properties of Mn PHEO and Al PHEO

Figure 5A shows the room temperature dielectric permittivity and loss tangent of Mn PHEO and Al PHEO films; Mn PHEO films are represented by a violet line, Al PHEO films are represented by an orange line. Mn PHEO exhibited a relative permittivity of ≈ 3000 at 100 Hz, but it decayed to 1500 at 100 kHz; the same trend was observed for the loss tangent. The frequency-

dependent dielectric properties were attributed to space charge contributions originating from charge hopping between different valence states of Mn ions. In contrast, Al PHEO showed frequency-independent dielectric properties with a relative permittivity of ≈2000 and a loss tangent <0.05 over the entire measure frequency range. The polarization loops (Figure 5B) of Al PHEO are very slim ferroelectric loops with low remanent polarization ($P_r = 7.1 \, \mu \text{C cm}^{-2}$) for a maximum applied electric field of 520 kV cm⁻¹. The low remanent polarization from Figure 5B implies that long-range polar order can effectively be destroyed due to the presence of five different elements on the B-site. As shown later, the presence of relaxor ferroelectricity suggests that there may be nanopolar regions.^[37,38] However, the Mn PHEO hysteresis loops are bloated and banana-shaped due to leakage, inflating the apparent remanent polarization. [39] Given the multivalency of Mn ions that adopts a mixture of 2+, 3+, and 4+ oxidation states, electron or hole hopping induces the bloated shape of the P-E loop for Mn PHEO in Figure 5B. However, Al has only a 3+ oxidation state available, so the resulting film is a good electrical insulator. Thus, the slim relaxor-like P–E loops of Al PHEO can be produced.

Positive-up and negative-down (PUND) measurements were performed to differentiate ferroelectric displacement currents from nonferroelectric currents. [40] For Mn PHEO, the PUND polarization was only 1.8 μ C cm⁻². Even though the Mn PHEO is electrically too conductive to be used in electrocaloric applications, the importance of the Mn PHEO can be underscored by the applicability of HEO-like formulations on Pb-based perovskites and the observation of the reversible cyclic phase transformation.

2.4. Temperature-Dependent Dielectric and Ferroelectric Properties of Al PHEO

The dielectric response of Al PHEO was measured as a function of temperature, as shown in **Figure 6**A. The maximum dielectric permittivity, $T_{\rm m}$, was 105 °C. The material showed stronger frequency dispersion below $T_{\rm m}$, and the data converged above this temperature. This is consistent with relaxor ferroelectric-like behavior for Al PHEO and it implies that polar entropy can be induced by multiple cations occupying the same lattice site. [37] There was some sample-to-sample variability in the permittivity values, even in cases where no differences could be observed in the X-ray patterns as shown in Figure S7

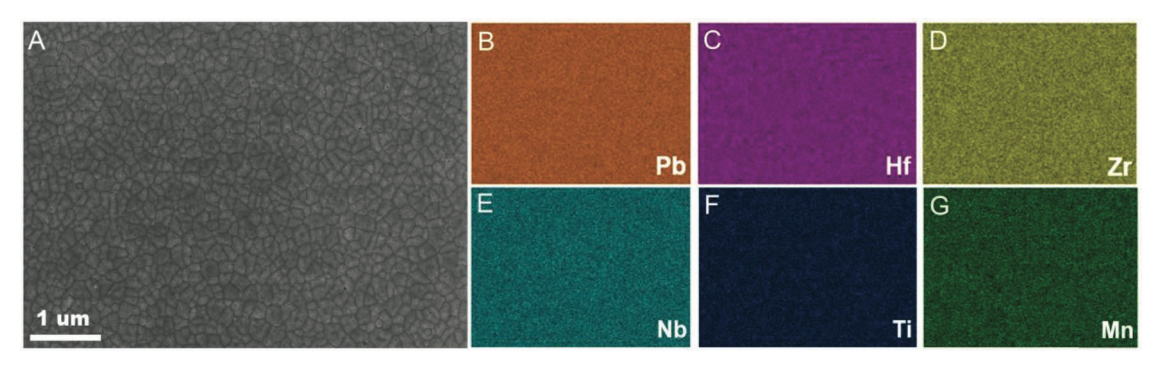


Figure 3. A) Field emission scanning electron microscope (FESEM) top view of a Mn PHEO film and B-G) EDS analysis to reveal homogeneity of the constituent elements.

2199160x, 2022, 12, Downloaded from https:

.com/doi/10.1002/aelm.202200352 by Pemsylvania State University, Wiley Online Library on [16/05/2023]. See the Terms and Conditions (https://on

of use; OA articles are governed by the applicable Creative Commons

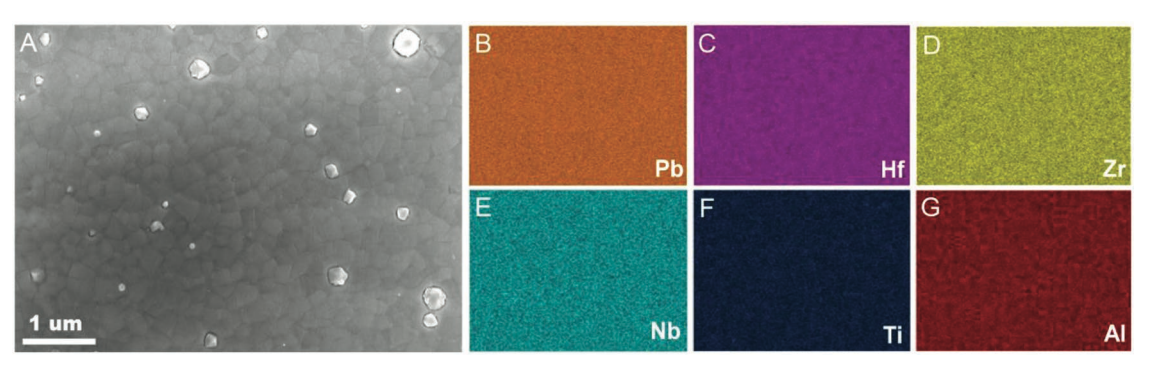


Figure 4. A) Field emission scanning electron microscope (FESEM) top view of an Al PHEO film and B-G) EDS analysis to reveal homogeneity of the constituent elements.

(Supporting Information). It is likely that these differences are sensitive to the defect chemistry.

The plot of inverse dielectric permittivity against temperature is presented in Figure 6B. It is obvious that there is a clear deviation from Curie–Weiss law between $T_{\rm m}$ and the Burns temperature $T_{\rm B}$, presumably due to the presence of polar nano regions (PNRs). [41] The relaxation behavior of Al PHEO is demonstrated via a modified Curie–Weiss law (Figure S8, Supporting Information):

$$\frac{1}{\varepsilon_{\rm r}} - \frac{1}{\varepsilon_{\rm m}} = \frac{(T - T_{\rm m})^{\gamma}}{C} \tag{1}$$

where ε_r is the dielectric permittivity, ε_m is the maximum dielectric permittivity, C is the Curie–Weiss constant, and γ is the degree of dielectric relaxation. The Curie–Weiss constant and relaxation constant is determined as 2.9×10^5 °C and 1.9, consistent with the presumption that Al PHEO contains a certain amount of relaxor ferroelectric character.

Figure 7A shows the ferroelectric loops of Al PHEO from – 30 °C to 220 °C. The maximum applied field was 1186 kV cm⁻¹, less than half of the breakdown field (3000 kV cm⁻¹), to avoid breakdown during measurement. Notably, the shape of the loop was maintained over the measured temperature range although

the P_{max} and P_{r} dropped by 6 and 8 $\mu\text{C cm}^{-2}$, respectively. Figure 7B shows the maximum polarization values as a function of temperature for electric fields from 0 to 1186 kV cm⁻¹. Above 260 °C, the apparent polarization was influenced by leakage currents, highlighted by the blue line. [42] The area highlighted by a red ellipse in Figure 7B represents a relatively sharp drop in remanent polarization due to the reduction of the long range polar order. [43] The lines connecting the polarization data points are 6th order polynomial fits, used for the calculation of electrocaloric effects based on Maxwell's relations. Figure S10 (Supporting Information) illustrates ferroelectric loops of Mn PHEO film measured from -30 °C to 120 °C temperature range. At -30 °C, the loop shape is similar to that of Al PHEO, a slim and relaxor-like P–E loop. However, the loops become more "banana-like" with increasing temperature due to the lossy characteristic of the Mn PHEO as discussed previously.[39] Therefore, it could not be exploited for the electrocaloric calculation.

2.5. Electrocaloric Effect of Al PHEO Film

To calculate the electrocaloric effects, the theoretical density of Al PHEO was determined using X-ray data, and the heat

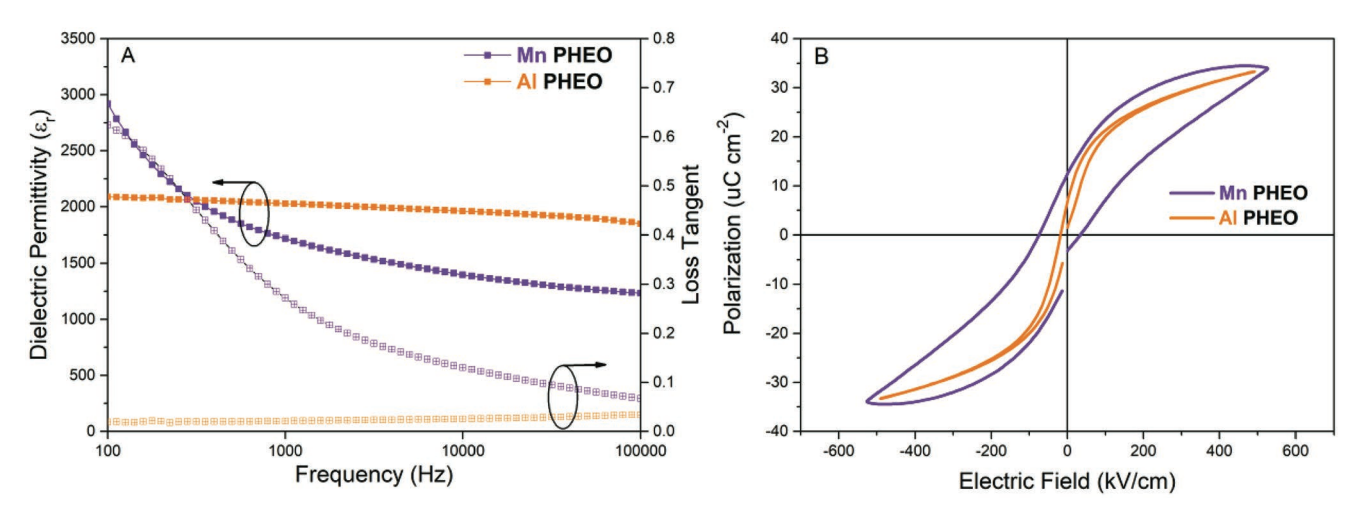


Figure 5. A) Dielectric permittivity and loss tangent. B) Ferroelectric hysteresis loops of the Mn PHEO (violet) and Al PHEO films (orange) measured at room temperature, respectively.

2199160x, 2022, 12, Downlo

com/doi/10.1002/aelm.202200352 by Pennsylvania State University, Wiley Online Library on [16/05/2023]. See the Terms and Conditions (https://onl

of use; OA articles are governed by the applicable Creative Commons

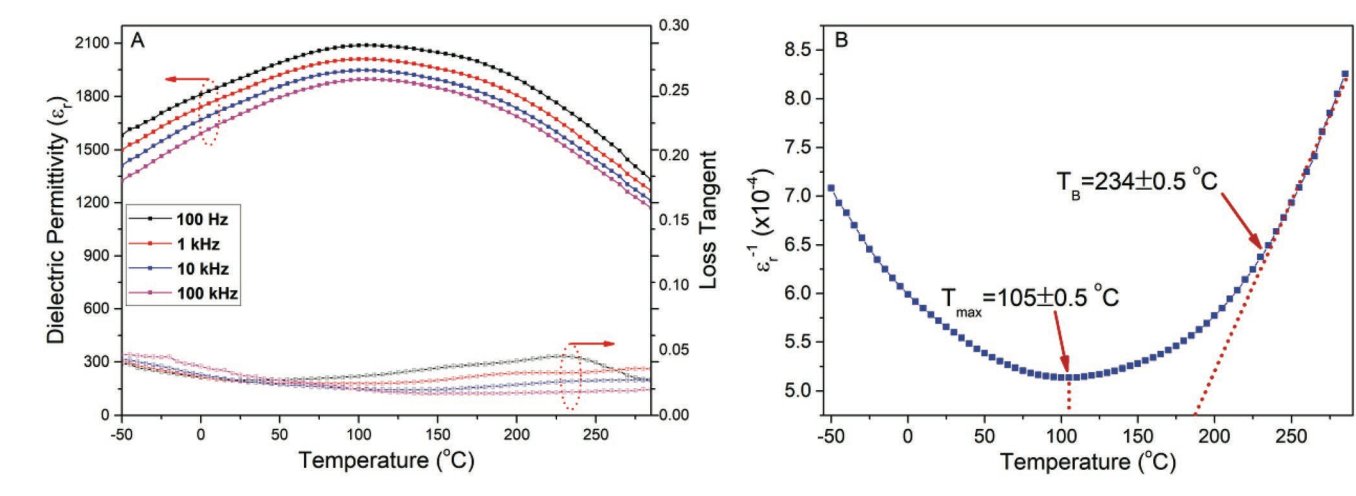


Figure 6. A) Dielectric permittivity and loss tangent of Al PHEO film from -50 °C to 280 °C at frequencies from 100 Hz to 100 kHz. B) Inverse dielectric permittivity versus temperature indicating a dielectric maxima at 105 °C and a Burns temperature of 234 °C. The red dotted line shows deviation from Curie–Weiss law below the Burns temperature.

capacity was assumed to be the same as reported values for PbMg_{1/3}Nb_{2/3}O₃ – PbTiO₃ (PMN-PT). [44] The electrocaloric temperature change ($\Delta T_{\rm ECE}$) and the associated entropy change ($\Delta S_{\rm ECE}$) are shown in **Figure 8**A,B, respectively. The maximum $\Delta T_{\rm ECE}$ of 8.4 K was obtained at 180 °C; the corresponding maximum $\Delta S_{\rm ECE}$ of 6.0 J Kg⁻¹K⁻¹ was obtained at 170 °C with 1186 kV cm⁻¹ applied electric field.

In the Al PHEO, two peaks were observed in the electrocaloric response, as has previously been reported in other relaxor ferroelectrics. [45–47] The first peak correlated with the loss of long range polar order. This long-range order can be reintroduced by large applied electric fields, inducing an increase in the field-induced entropy change. As the temperature approached the dielectric maximum, field-induced switching of local polar order was facilitated by thermal fluctuations. This established the second peak in the electrocaloric responses, which was maximized at 180 °C. Above this temperature, the electrocaloric response dropped and thermal randomization of the dipoles

reduced the alignment. When the temperature reached $T_{\rm B}$, the local polar order disappeared, producing a sharp drop of $\Delta T_{\rm ECE}$. The electrocaloric temperature change of the Al PHEO film is not as high as a recently proposed high entropy polymer. However, it reveals a comparable temperature change to other oxide-based materials with a relatively wide working temperature range.

3. Conclusions

For powder processing, Mn PHEO can be obtained at 750 °C in 240 min with a minor amount of second phase formation. Mn PHEO powder undergoes entropy-driven phase transformation. However, Al PHEO powder is not phase-pure under the same processing conditions. Mn and Al PHEO films were synthesized by PLD; their dielectric and ferroelectric properties were investigated and electrocaloric effect was evaluated based on the

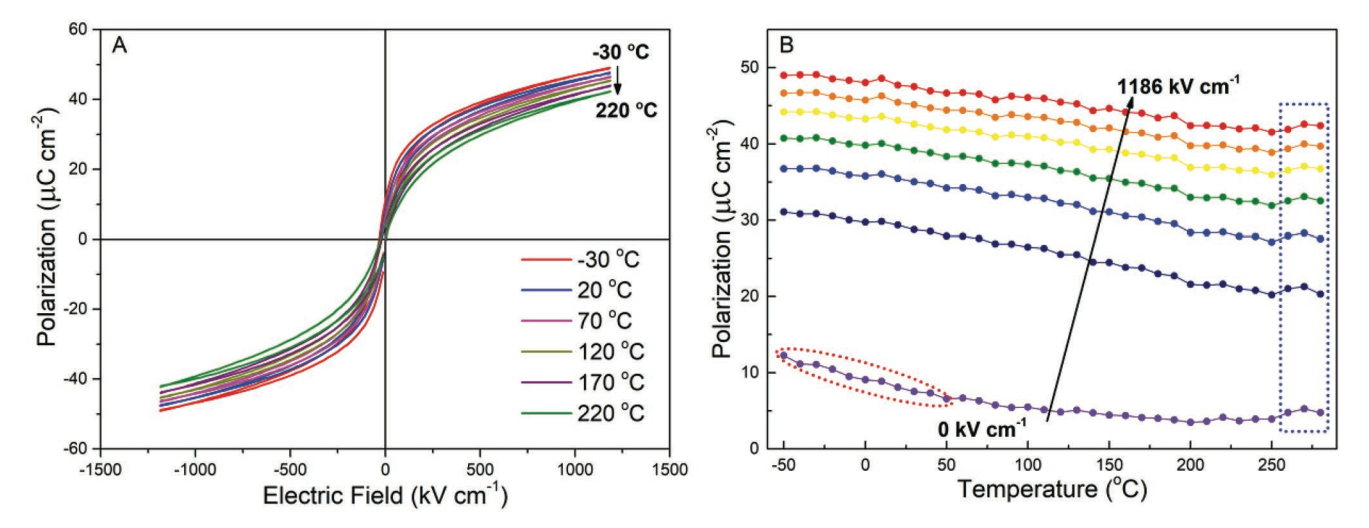


Figure 7. A) Ferroelectric hysteresis loops measured from −30 °C to 220 °C. B) Maximum polarizations at different electric fields from 0 to 1186 kV cm⁻¹ from −50 °C to 280 °C with 10 °C intervals.

2199160x, 2022, 12, Downloaded from https:

.com/doi/10.1002/aelm.202200352 by Pennsylvania State University, Wiley Online Library on [16/05/2023]. See the Terms and Conditions (https://onlinelibrary.wiley./

ns) on Wiley Online Library for rules of use; OA articles are governed by the applicable Creative Commons I

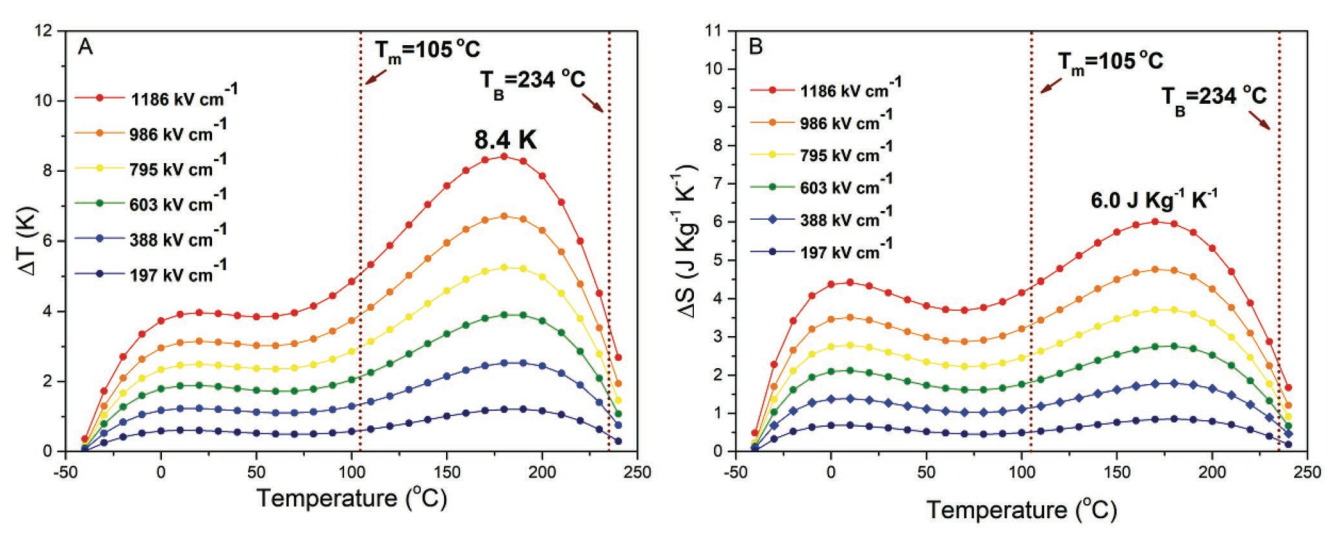


Figure 8. A) Electrocaloric temperature change of the Al PHEO. $\Delta E = E_2 - E_1$ where E_2 is fixed as 1186 kV cm⁻¹. Blue dotted lines are T_m and T_B , respectively. B) Corresponding entropy change of Al PHEO.

Maxwell relations. Phase-pure Mn PHEO films were achieved; in Al PHEO films, a small amount of pyrochlore was detected under similar processing conditions. Mn PHEO films were electrically leaky, presumably due to mixed valence on the Mn ions. In contrast, Al PHEO films were insulating and exhibited relative dielectric permittivities of 2000 with loss tangents <0.05 at room temperature. Slim relaxor ferroelectric hysteresis loops were observed with $P_{\rm max}$ of 47.7 $\mu {\rm C~cm^{-2}}$ and $P_{\rm r}$ of 8.2 $\mu {\rm C~cm^{-2}}$ at room temperature, with dielectric relaxation below $T_{\rm m}$ and progressive loss of the dispersion above $T_{\rm m}$. The maximum indirect electrocaloric temperature change was 8.4 K at 180 °C with an applied electric field of 1186 kV cm $^{-1}$.

4. Experimental Section

Target Preparation: To fabricate a ceramic Pb(Hf_{0.2}Zr_{0.2}Ti_{0.2}Nb_{0.2}Mn_{0.2}) O₃ target, a Mn-based B-site precursor was mixed using HfO₂ (Stanford Materials Corp, (99.9%), ZrO₂ (Alfa Aesar, 99.7%), TiO₂ (Alfa Aesar, 99.7%), Nb₂O₅ (Alfa Aesar, 99.9%), and Mn₂O₃ (Alfa Aesar, 98.0%) powders that were wet ball-milled with ethanol for 12 h. The resultant slurry was then dried at 80 °C for >24 h. The dried powder was calcined at temperatures from 1000 °C to 1400 °C for 240 min to homogenize the cation distribution and attempt to form a single-phase $Hf_{0.2}Zr_{0.2}Ti_{0.2}Nb_{0.2}Mn_{0.2}O_x$ (Mn precursor), following a columbite-like route.[31] However, despite multiple calcination, crushing, calcination cycles, single-phase precursors were not achieved up to 1400 °C. After adding Pb₃O₄ (Sigma-Aldrich, 99%), single phase Pb(Hf_{0.2}Zr_{0.2}Ti_{0.2}Nb_{0.2}Mn_{0.2})O₃ perovskite was obtained with a calcination step at 750 °C for 240 min. After calcination, the powder was vibratory milled with 20 mol% excess PbO and pressed into a 1-inch pellet in a uniaxial press, followed by cold isostatic pressing (CIP). The pressed pellet was sintered at 850 °C for 120 min. The finished pellet was used as a target for PLD. A comparable procedure was used to make the Al-based PHEO target (Alfa Aesar, 99.0%), however, a singlephase was not achieved.

Film Deposition: Perovskite high entropy oxide thin films were synthesized using a KrF (248 nm) excimer laser (Compex 102 F, Coherent). For all growths, the laser energy density and substrate-target distance were fixed at 1.15 \pm 0.04 J cm $^{-2}$ and 40 mm, unless otherwise specified. The optimization process was carried out under varying

deposition pressures, laser frequencies, and substrate temperatures for growth on Pt/Ti/SiO $_2$ /Si substrates (KOTech LLC) with a 60 nm Nb-doped PZT seed layer. $^{[48,49]}$ Mn PHEO films were synthesized with 175 mTorr, $90\%O_3/10\%O_2$ deposition ambient, at a 630 °C substrate temperature and 10 Hz laser frequency. Identical processing conditions were used for Al PHEO films.

Structural Characterization: The phase purity and crystallographic orientation of the film was assessed using a PANalytical Empyrean diffractometer with Cu K α X-ray radiation. The microstructures of the films were observed with a Merlin Field Emission Scanning Electron Microscope (FESEM) (Carl Zeiss Microscopy GmbH, Hena, Germany). Film compositions were characterized by energy dispersive X-ray spectroscopy (AZtecLive Advanced Microanalysis system with an UltiMax 100 SSD Detector). A spectroscopic ellipsometer (Woollam M-2000 XF-193) was used to map the thickness uniformity of the sample (Figure S9, Supporting Information).

Electrical Characterization: To characterize the electrical properties, platinum (Pt) top electrodes varying from 200 to 15 μm in diameter were prepared by double-layer resist photolithography and a lift-off process. 100 nm thick Pt electrodes were sputter deposited on the PHEO films (CMS-18 sputter system, Kurt J. Lesker Company, Pittsburgh, PA) over the resist stack. After lift-off, rapid thermal annealing was performed at 500 °C for 1 min to improve the contact between the Pt electrodes and the film. To expose the bottom electrode, 1827 (Shipley) photoresist was coated on the sample, defining the area for etching. After curing at 95 °C for 3 min, a 10:1 buffered HF etch was followed by a hydrochloric acid etch to remove the PHEO film. Finally, the photoresist was removed by acetone. To validate the quality of the top electrode patterning, the dielectric properties of Al PHEO were measured for various electrode sizes, as displayed in Figure S6 (Supporting Information).

Dielectric Property and Ferroelectric Property Measurement: An HP 4284 LCR meter was used to measure the room temperature dielectric property of the films from 100 Hz to 100 kHz with 30 mV applied to a 200 µm diameter top electrode. Polarization-electric field hysteresis loops were obtained using a Precision Multiferroic tester (Radiant Technology) at 10 kHz. The temperature-dependent dielectric measurement was performed with either an in-house probe station (Love_Film Stage) or a FormFactor 11 000 from -50 °C to 285 °C. An AC voltage of 100 mV was applied to the top electrode from 100 Hz to 1 MHz.

Electrocaloric Entropy and Temperature Change Calculation: To calculate the electrocaloric entropy and temperature changes, an indirect measurement approach based on Maxwell's relations was applied. The upper branches of the P–E loops were measured and fitted to a sixth order polynomial at temperatures from $-50\,^{\circ}\text{C}$ to 280 $^{\circ}\text{C}$. A temperature

interval of $10\,^{\circ}\text{C}$ was adopted to reduce peak shifts as reported elsewhere.^[50] Numerical differentiation of the P(T) values was used as input Equations (2) and (3).

$$\Delta T = -\frac{T}{\rho C_p} \int_{E}^{E_2} \left(\frac{dP}{dT}\right)_E dE \tag{2}$$

$$\Delta S = -\frac{1}{\rho} \int_{E}^{E_{2}} \left(\frac{dP}{dT} \right)_{E} dE \tag{3}$$

where ρ is the mass density of the material, C_p is the specific heat capacity, P is the polarization, T is the measured temperature, and E_1 and E_2 are the initial and final applied electric fields, respectively. The theoretical density of Al PHEO determined by XRD was used and the heat capacity was assumed to be the same as that of PbMg_{1/3}Nb_{2/3}O₃ – PbTiO₃ (PMN-PT).

Supporting Information

Supporting Information is available from the Wiley Online Library or from the author.

Acknowledgements

The authors gratefully acknowledge support from National Science Foundation through the Pennsylvania State University Materials Research Science and Engineering Center DMR-2011839. The authors would also like to acknowledge Beth Jones and Nichole Wonderling for the target preparation and discussion on XRD peak analysis, respectively.

Conflict of Interest

The authors declare no conflict of interest.

Data Availability Statement

The data that supports the finds of this study are available from the corresponding author upon reasonable request.

Keywords

electrocaloric effect, entropy-driven phase transformation, high entropy oxides, perovskite structures, pulsed laser deposition, thin films

Received: March 28, 2022 Revised: August 26, 2022 Published online: September 20, 2022

- [1] S. Chu, A. Majumdar, Nature 2012, 488, 294.
- [2] Annual Energy Outlook 2016 With Projections to 2040, Vol. 08, 2016.
- [3] M. Veselý, W. Zeiler, Renewable Sustainable Energy Rev. 2014, 34, 401.
- [4] P.-C. Hsu, X. Liu, C. Liu, X. Xie, H. R. Lee, A. J. Welch, T. Zhao, Y. Cui, Nano Lett. 2014, 15, 365.
- [5] S. Hong, Y. Gu, J. Seo, J. Wang, P. Liu, Y. Meng, S. Xu, R. Chen, Sci. Adv. 2019. 5, 0536.
- [6] I. Chowdhury, R. Prasher, K. Lofgreen, G. Chrysler, S. Narasimhan, R. Mahajan, D. Koester, R. Alley, R. Venkatasubramanian, *Nat. Nanotechnol.* 2009, 4, 235.

- [7] J. Athavale, M. Yoda, Y. Joshi, Adv. Heat Transfer 2018, 50, 123.
- [8] 2015 International Technology Roadmap for Semiconductors (ITRS), Semiconductor Industry Association, Wasington, DC 2015.
- [9] M. Pedram, S. Nazarian, Proc. IEEE 2006, 94, 1487.
- [10] S. M. Sohel Murshed, C. A. Nieto de Castro, Renewable Sustainable Energy Rev. 2017, 78, 821.
- [11] X. Moya, S. Kar-Narayan, N. D. Mathur, Nat. Mater. 2014, 13, 439.
- [12] S. G. Lu, Q. Zhang, Adv. Mater. 2009, 21, 1983.
- [13] J. Mao, G. Chen, Z. Ren, Nat. Mater. 2021, 20, 454.
- [14] A. Mischenko, Q. Zhang, J. Scott, R. Whatmore, N. Mathur, Science 2006, 311, 1270.
- [15] J. F. Scott, Annu. Rev. Mater. Res. 2011, 41, 229.
- [16] E. Defay, R. Faye, G. Despesse, H. Strozyk, D. Sette, S. Crossley, X. Moya, N. D. Mathur, Nat. Commun. 2018, 9, 1827.
- [17] S. G. Lu, B. Rožič, Q. M. Zhang, Z. Kutnjak, X. Li, E. Furman, L. J. Gorny, M. Lin, B. Malič, M. Kosec, R. Blinc, R. Pirc, Appl. Phys. Lett. 2010, 97, 162904.
- [18] B. Cantor, I. T. H. Chang, P. Knight, A. J. B. Vincent, *Mater. Sci. Eng.*, A 2004, 375–377, 213.
- [19] J. W. Yeh, S. K. Chen, S. J. Lin, J. Y. Gan, T. S. Chin, T. T. Shun, C. H. Tsau, S. Y. Chang, Adv. Eng. Mater. 2004, 6, 299.
- [20] C. M. Rost, E. Sachet, T. Borman, A. Moballegh, E. C. Dickey, D. Hou, J. L. Jones, S. Curtarolo, J.-P. Maria, *Nat. Commun.* 2015, 6, 8485.
- [21] D. Bérardan, S. Franger, D. Dragoe, A. K. Meena, N. Dragoe, Phys. Status Solidi RRL 2016, 10, 328.
- [22] D. Bérardan, S. Franger, A. K. Meena, N. Dragoe, J Mater Chem 2016, 4, 9536.
- [23] J. Gild, M. Samiee, J. Braun, T. Harrington, H. Vega, P. Hopkins, K. Vechio, J. Luo, J. Eur. Ceram. Soc. 2018, 38, 3578.
- [24] A. Sarkar, B. Breitung, H. Hahn, Scr. Mater. 2020, 187, 43.
- [25] Y. Pu, Q. Zhang, R. Li, M. Chen, X. Du, S. Zhou, Appl. Phys. Lett. 2019, 115, 223901.
- [26] W. Liu, F. Li, G. Chen, G. Li, H. Shi, L. Li, Y. Guo, J. Zhai, C. Wang, J. Mater. Sci. 2021, 56, 18417.
- [27] S. Wei, X. Chen, G. Dong, L. Liu, Q. Zhang, B. Peng, Ceram. Int. 2022. 48. 15640.
- [28] X. Qian, D. Han, L. Zheng, J. Chen, M. Tyagi, Q. Li, F. Du, S. Zheng, X. Huang, S. Zhang, J. Shi, H. Huang, X. Shi, J. Chen, H. Qin, J. Bernholc, X. Chen, L. Q. Chen, L. Hong, Q. M. Zhang, *Nature* 2021, 600, 664.
- [29] D. J. Singh, M. Ghita, S. V. Halilov, M. Fornari, J. Phys. IV 2005, 128, 47.
- [30] R. E. Cohen, Nature 1992, 358, 136.
- [31] S. L. Swartz, T. R. Shrout, Mater. Res. Bull. 1982, 17, 1245.
- [32] J. Nelson, D. P. Riley, Proc. Phys. Soc. 1945, 57, 160.
- [33] H. Serier-Brault, M. Jansen, Solid State Sci. 2011, 13, 326.
- [34] R. D. Shannon, Acta Crystallogr. Sect. A: Found. Adv. 1976, 32, 751.
- [35] L.-X. He, C.-E. Li, J. Mater. Sci. 2000, 35, 2477.
- [36] G. Li, L. Zheng, Q. Yin, B. Jiang, W. Cao, J. Appl. Phys. 2005, 98, 064108.
- [37] F. Li, S. Zhang, D. Damjanovic, L.-Q. Chen, T. R. Shrout, F. Li, S. Zhang, L.-Q. Chen, T. R. Shrout, S. J. Zhang, D. Damjanovic, Adv. Funct. Mater. 2018, 28, 1801504.
- [38] C. A. Randall, A. S. Bhalla, T. R. Shrout, L. E. Cross, J. Mater. Res. 1990, 5, 829.
- [39] J. F. Scott, J. Phys.: Condens. Matter 2007, 20, 021001.
- [40] S. Martin, N. Baboux, D. Albertini, B. Gautier, Rev. Sci. Instrum. 2017, 88, 023901.
- [41] R. A. Cowley, S. N. Gvasaliya, S. G. Lushnikov, B. Roessli, G. M. Rotaru, Adv. Phys. 2011, 60, 229.
- [42] B. Peng, T. Wang, L. Liu, X. Chen, J. Li, Q. Zhang, R. Yang, W. Sun, Z. L. Wang, Nano Energy 2021, 86, 106059.
- [43] J. Li, J. Li, S. Qin, X. Su, L. Qiao, Y. Wang, T. Lookman, Y. Bai, Phys. Rev. Appl. 2019, 11, 044032.



2199160x, 2022, 12. Downloaded from https://onlinelibrary.wiley.com/doi/10.1002/aelm.202200352 by Pennsylvania State University, Wiley Online Library on [16/05/2023]. See the Terms

conditions) on Wiley Online Library for rules of use; OA articles are governed by the applicable Creative Commons License

- [44] M. V. Gorev, I. N. Flerov, V. S. Bondarev, P. Sciau, J. Exp. Theor. Phys. 2003, 96, 531.
- [45] B. Peng, H. Fan, Q. Zhang, Adv. Funct. Mater. 2013, 23, 2987.
- [46] G. Chen, Y. Zhang, X. M. Chu, G. Zhao, F. Li, J. Zhai, Q. Ren, B. Li, S. Li, J. Alloys Compd. 2017, 727, 785.
- [47] J. Hagberg, A. Uusimäki, H. Jantunen, Appl. Phys. Lett. 2008, 92, 132909.
- [48] T. Borman, W. Zhu, K. Wang, S. Ko, P. Mardilovich, S. E. Trolier-McKinstry, J. Am. Ceram. Soc. 2017, 100, 3558.
- [49] W. Zhu, B. Akkopru-Akgun, J. I. Yang, C. Fragkiadakis, K. Wang, S. W. Ko, P. Mardilovich, S. Trolier-McKinstry, Acta Mater. 2021, 219, 117251.
- [50] Y. Liu, J. F. Scott, B. Dkhil, Appl. Phys. Rev. 2016, 4, 064109.